

JGR Planets

RESEARCH ARTICLE

10.1029/2020JE006686

Key Points:

- In 2018–2020, Jupiter's Great Red Spot interacted with series of anticyclones, losing part of its visible red area and distorting its shape
- The Great Red Spot (GRS) increased its tangential velocity; it did not change its vorticity, but did temporarily change its 90-day oscillation in longitude
- Dynamical and radiative transfer modeling shows that the interactions affected the upper cloud of the GRS with no risk for its survival

Supporting Information:

- Supporting Information S1

Correspondence to:

A. Sánchez-Lavega,
agustin.sanchez@ehu.eus

















Citation:

Sánchez-Lavega, A., Anguiano-Arteaga, A., Iñurrigarro, P., García-Melendo, E., Legarreta, J., Hueso, R., et al. (2021). Jupiter's Great Red Spot: Strong interactions with incoming anticyclones in 2019. *Journal of Geophysical Research: Planets*, 126, e2020JE006686. <https://doi.org/10.1029/2020JE006686>

Received 8 SEP 2020

Accepted 23 FEB 2021

Jupiter's Great Red Spot: Strong Interactions With Incoming Anticyclones in 2019

A. Sánchez-Lavega¹ , A. Anguiano-Arteaga¹ , P. Iñurrigarro¹, E. García-Melendo² , J. Legarreta¹, R. Hueso¹ , J. F. Sanz-Requena^{3,4} , S. Pérez-Hoyos¹ , I. Mendikoa⁵ , M. Soria² , J. F. Rojas¹ , M. Andrés-Carcasona² , A. Prat-Gasull² , I. Ordoñez-Extebarria¹, J. H. Rogers⁶, C. Foster⁷, S. Mizumoto⁸ , A. Casely⁹ , C. J. Hansen¹⁰ , G. S. Orton¹¹ , T. Momary¹¹ , and G. Eichstädt¹²

¹Escuela de Ingeniería de Bilbao, Universidad del País Vasco UPV/EHU, Bilbao, Spain, ²Universitat Politècnica de Catalunya UPC, Terrasa, Spain, ³Universidad Europea Miguel de Cervantes, Valladolid, Spain, ⁴Dpto. Física Teórica, Atómica y Óptica, Universidad de Valladolid, Valladolid, Spain, ⁵Tecnalia Research and Innovation, Bilbao, Spain, ⁶British Astronomical Association, London, UK, ⁷Astronomical Society of Southern Africa, Centurion, South Africa, ⁸Association of Lunar and Planetary Observers ALPO-Japan, Chofu, Japan, ⁹Independent Scholar, Sydney, Australia, ¹⁰Planetary Science Institute, Tucson, AZ, USA, ¹¹Jet Propulsion Laboratory, California Institute of Technology, Pasadena, CA, USA, ¹²Independent Scholar, Stuttgart, Germany

Abstract Jupiter's Great Red Spot (GRS), a giant anticyclone, is the largest and longest-lived of all the vortices observed in planetary atmospheres. During its history, the GRS has shrunk to half its size since 1879, and encountered many smaller anticyclones and other dynamical features that interacted in a complex way. In 2018–2020, while having a historically small size, its structure and even its survival appeared to be threatened when a series of anticyclones moving in from the east tore off large fragments of the red area and distorted its shape. In this work, we report observations of the dynamics of these interactions and show that as a result the GRS increased its internal rotation velocity, maintaining its vorticity but decreasing its visible area, and suffering a transient change in its otherwise steady 90-day oscillation in longitude. From a radiative transfer analysis and numerical simulations of the dynamics we show that the interactions affected the upper cloud tops of the GRS. We argue that the intense vorticity of the GRS, together with its larger size and depth compared to the interacting vortices, guarantees its long lifetime.

Plain Language Summary Jupiter's Great Red Spot (GRS) is a giant anticyclone with a length that has shrunk since 1879 from ~ 40,000 km to its current value of 15,000 km. The GRS is the longest-lived of all the planetary vortices, observed perhaps since the 17th century. During its history, the GRS has encountered a variety of smaller anticyclones and other dynamical features, surviving these interactions. In 2018–2020, a series of anticyclones interacted with it, and tore off large fragments of its red area (called “flakes”), eroding and distorting its oval shape, and apparently threatening its survival. The interactions produced an increase in the GRS internal rotation velocity accompanied by a transient increase in the period and amplitude of its steady 90-day oscillation in longitude. From the analysis of the reflectivity of the GRS and flakes and model simulations of the dynamics of the interactions we find that these events are likely to have been superficial, not affecting the full depth of the GRS. The interactions are not necessarily destructive but can transfer energy to the GRS, maintaining it in a steady state and guaranteeing its long lifetime.

1. Introduction

Jupiter's Great Red Spot (GRS) is the archetype and the best studied of all the vortices in the giant planets, but its origin and fate remain mysterious. The first detailed studies of this anticyclone started with the Voyager 1 and 2 flybys in 1979, when its velocity field, vorticity and temperature structure at the upper cloud level were measured (Conrath et al., 1981; Flasar et al., 1981; Mitchell et al., 1981). Over the past 130 years, the GRS has decreased in size by half (Rogers, 1995; Simon et al., 2018) and has undergone numerous interactions with a variety of different dynamical features (anticyclonic vortices and open circulating cells called South Tropical Disturbances, STrD) that develop at its latitude east and west of its location (Li et al., 2004;

Rogers, 1995; Sada et al., 1996; Sánchez-Lavega et al., 1998, 2013; Smith et al., 1979). Encounters of smaller anticyclonic vortices (AV) similar to those described here with the GRS were observed in image sequences from the Voyager 1 flyby in 1979 (Rogers, 1995; Sada et al., 1996; Smith et al., 1979). At that time, the GRS was large and exhibited a complex cloud morphology, and apparently was less disrupted by the interactions, although some AV material was eventually pulled into the GRS.

Throughout 2018–2020, a series of interactions took place between the GRS and AVs coming from the east, as described in detail in previous cases (Li et al., 2004; Sánchez-Lavega et al., 1998; Smith et al., 1979). The new events here studied were particularly interesting for three reasons. First, the GRS at the time had the smallest size in its history. Second, the vortices had a medium size, $\sim 2.5\%$ – 5% of the GRS area, and were numerous, such that they collided with the GRS one after another. Third, the encounters gave rise to strong interactions of a type rarely recorded before. All this significantly disrupted the red oval area of the GRS, and was even suspected of putting its long life at risk.

2. Materials and Methods

An alert was circulated by the amateur community early in 2019 on the GRS events (nicknamed “flakes”) and a large number of images were gathered during that year by observers contributing to open planetary image repositories such as Planetary Virtual Observatory and Laboratory (PVOL) database (Hueso et al., 2018). See Table S1 for a full list of observations used (Sánchez-Lavega, 2021). Additional images in the visual and near-infrared spectral ranges were obtained from May 27 to 30, 2019 with the 2.2 m telescope at Calar Alto Observatory using the instrument PlanetCam (Mendikoa et al., 2016) that were photometrically calibrated (Mendikoa et al., 2017) and used for a radiative transfer analysis. We also used observations obtained in 2018–2020 with JunoCam on the Juno spacecraft and with the Hubble Space Telescope (HST; Table S2). We focus in this study on the epochs when most active interaction episodes occurred from May to July 2019 (Table S2).

2.1. Measurement of Ground-Based Images

We used the software WinJupos to navigate images from telescopic observations, map-project them and measure the positions of features (WinJupos, 2020). The motions of the features were measured in two ways: (1) When the displacements were short in time and the trajectory could be considered a straight line in longitude or latitude, we used series of images to track the motion (a minimum is always an image pair), limited by the spatial resolution and time interval, then making a linear fit to retrieve their mean drift rate (degrees/day) in latitude and longitude, and converting displacements into zonal and meridional velocities; (2) when the trajectory was curved, for each feature used as a tracer, its position (latitude and longitude relative to the center of the GRS) was calculated for each time measured and drawn on the map. In most cases, this trajectory was well represented by the arc of an ellipse in correspondence with the GRS flow. We then superimposed an ellipse to the points representing the trajectory of the feature in the longitude-latitude map and manually fitted the track with a pointer to adjust the center of the ellipse and determine its minor and major axis. We then calculated the length of the arc of the ellipse traced by the motion of the feature and retrieved the average velocity after dividing by the time interval between the first and last dates that determine the trajectory. This method was used for motions both inside and outside the red oval.

A lower limit to the errors in wind measurements retrieved from features tracking in ground-based images can be estimated as the image resolution divided by the tracking time $\sim 400\text{--}600\text{ km}/(20\text{ h}) \sim 5\text{--}10\text{ ms}^{-1}$. The measurements of the position of the features was obtained when the GRS is at a distance $<45^\circ$ from the central meridian (CM). Only on particular occasions were measurements made with the GRS up to 60° from the cm. The combined errors of image navigation (position of the planet's disk using the WinJupos software) and pointing of features are in such cases $\sim 0.5^\circ$ ($\sim 570\text{ km}$ on the GRS). The temporal separation between the images used to trace the motion of a particular feature (sometimes on several images) is typically between 0.4 days and 1.2 day, reaching in some cases 3 days. For a time interval of 0.5 days of time interval, the error in speed associated with navigation and pointing of a feature moving at 150 ms^{-1} through the ellipse that draws the contour of the red spot turns out to be 15 ms^{-1} . Other estimates of velocity errors are presented in sections 3.1 and 3.2.

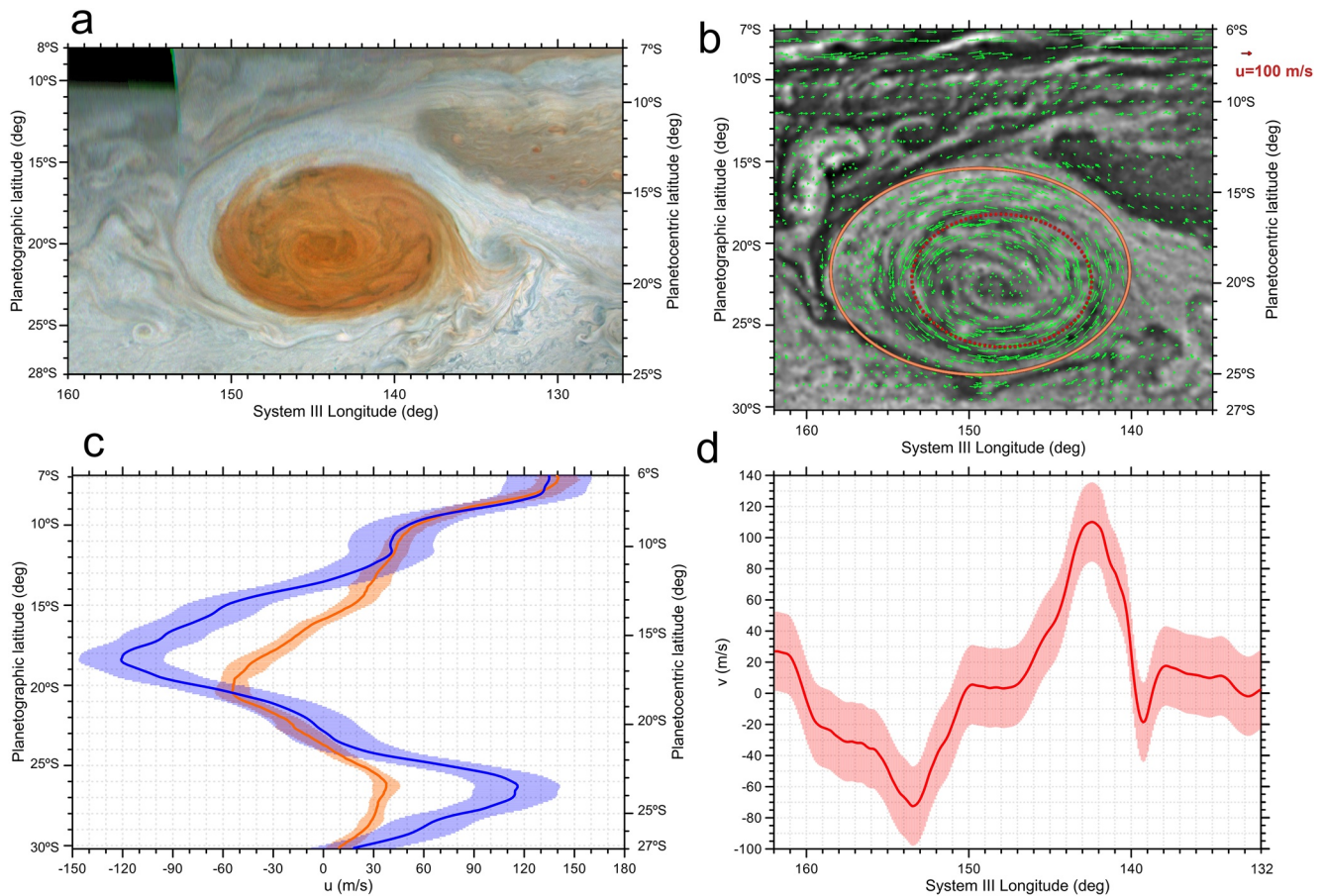


Figure 1. The GRS cloud morphology and wind field from HST images on April 17, 2018. (a) HST/WFC3 color composite image (filters: F395 N –blue-, F502 N –green-, F631 N –red-) obtained at 14:02:02U.T. average images time (OPAL program, Simon et al., 2015); (b) Image obtained in filter 631 nm with superimposed measured wind vectors. The ellipses enclose the location of maximum wind speeds (internal, dashed red) and the full GRS flow (external, orange); (c) Averaged zonal wind profile along the North-South major axis of the GRS (blue line with velocity uncertainty shadowed) compared to the mean zonal velocity profile (orange line); (d) Averaged wind profile along the east-west major axis of the GRS. The GRS red oval is centered at planetographic latitude $22.6^{\circ}\text{S} \pm 0.4^{\circ}$. Panel (a) shows in its interior similar features (in particular dark round and elongated spots) to those described in detail in 2017 (Sánchez-Lavega et al., 2018). Surrounding it there is a white ring (wider in the northern part, a region historically called the “hollow”). The GRS anticyclonic flow encompasses both regions (red oval and hollow) as can be seen from the wind field measurements (Figure 1b). A comparison with the ambient winds shows the correlation with the jet peaks and dynamical extent of the GRS (Figure 1c). In the north edge of the hollow, there is a discontinuity or gap at approximate latitude 10°S and longitude 141°III (Figure 1a), an opening in the circulation that allows the fluid elements to escape from the hollow in the northeast direction where they are carried eastward by the ambient zonal flow (Sánchez-Lavega et al., 1998). This gap is limited to the east by a stagnation region of low-albedo clouds (latitude 13°S , 138°III , Figure 1a; Sánchez-Lavega et al., 2018). The gap and stagnation regions form and disappear over time and affect the AV interaction with the GRS. See in Figure 7, the identification of these features. Planetographic latitudes and System III West longitudes are used throughout this article. AV, anticyclonic vortices; GRS, Great Red Spot; HST, Hubble Space Telescope; OPAL, Online Programs for Applied Learning.

2.2. Measurement of HST Images

The original images were navigated and projected into cylindrical maps using the WinJUPOS software (WinJupos, 2020). Maps were corrected for limb-darkening effects using a Lambert law and the contrast of features was enhanced using high-pass image filters. Then we used the PICV (Particle Image Correlation Velocimetry) image correlation software (Hueso et al., 2009; Hueso, 2020) to track the motions of cloud features from measurements of the displacement of features in pairs of HST images separated by 1.59 h. The software examined correlation of square subimages with square sides of 1° – 3° depending on the features location in different areas of the images. Most of the measurements were made with subimages of $1^{\circ} \times 1^{\circ}$ or $1.2^{\circ} \times 1.2^{\circ}$. All measurements (3,253 individual wind vectors in Figure 1) were validated by a human operator who visually checked each individual identification and correlation map produced by the software. To compute a continuous velocity field we interpolated the wind vectors into a regular grid of 0.1°

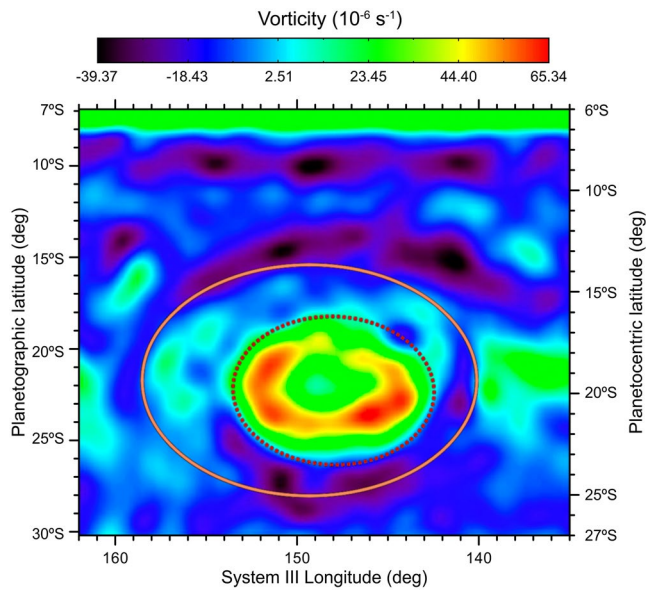


Figure 2. Relative vorticity map of the GRS. Values of the relative vorticity obtained from the velocity measurements presented in Figure 1b. The ellipses correspond to those drawn on the map in Figure 1b. The blue blob at planetographic latitude 19°S and longitude 145° is an artifact from the lack of measurements in that area. The methodology followed to calculate the relative vorticity and its precision is explained in detail in Hueso et al. (2009). GRS, Great Red Spot.

and smoothed to a resolution of 1° . This wind field was used to compute the mean zonal and meridional profiles along the center of the GRS (Figure 1) and the relative vorticity field (Figure 2).

We calculate velocity errors of 25 ms^{-1} due to the initial resolution of the images and time difference of the image pair used. The statistical differences between close wind vectors or from extracting the zonal and meridional cuts from nearby latitudes are typically 2–3 times below this limit, supporting this estimation. Different plots of the values of the original vectors and the interpolated wind field have differences that are significantly lower than 25 ms^{-1} (which is the error bar appearing in Figures 1c and 1d). The spatial derivatives of the wind field needed to compute the vorticity map in Figure 2 are done with a spatial resolution of 1.2° formally resulting in an uncertainty in the values of the vorticity of $2 \times 10^{-5} \text{ s}^{-1}$, which is five times lower than the vorticity range displayed in this figure.

2.3. Mapping JunoCam Images

The raw JunoCam images were taken from the Reduced Data Record (RDR) product and have been corrected from the instrumental effects and adjusted for scaled levels of radiance (Caplinger, 2016). The image processing, map projection and navigation of the images was carried out using the ISIS software (Integrated Software for Imagers and Spectrometers) using the Juno trajectories available in SPICE kernels (Acton et al., 2016). After projecting each sector that makes up the image, we grouped all of them into a final map using the Geospatial Data Abstraction software libraries (GDAL/OGR, 2020). Finally, we combined the different filtered Red, Green and Blue images to the resulting color RGB

image. Further details on the navigation of details of JunoCam images and maps of the GRS are given in (Sánchez-Lavega et al., 2018 and references therein).

2.4. Radiative Transfer Analysis

Data obtained from PlanetCam-UPV/EHU for the two regions of interest at two similar geometrical configurations were photometrically calibrated in absolute reflectivity using calibration standard stars (SP1741 + 054 or Kopff-27 and HD84937 for the visible; HD102870 for visible and SWIR wavelengths) (Mendikoa et al., 2017). The spectral dependence of reflectivity was modeled with the NEMESIS code (Irwin et al., 2008; Irwin, 2020), which uses the optimal estimator scheme to retrieve the most likely atmospheric parameters that best fit the observed reflectivity. We assume Jupiter's atmosphere to be a mixture of H_2 and He, which produce Rayleigh scattering, and CH_4 , which has strong absorption bands in this wavelength range. Assumed abundances in volume mixing ratio were 0.835, 0.16 and 7×10^{-4} , respectively (Taylor et al., 2004). Methane absorption was added as pre-computed correlated-k tables from previous absorption coefficients widely used (Karkoschka & Tomasko, 2010). Further details are given in section 3.3.

3. Results from the Observations

Figure 1 puts in context the GRS cloud morphology and dynamics in April 2018, one year before the period of the strongest interactions, from images taken with the HST. At this time, a South Tropical Disturbance (STrD) was streaming eastwards past the GRS (Rogers et al., 2018). Dark spots from the STrD passed south of the GRS interacting with it on the eastern side forming streamers of red clouds (Figures 1a, 3 and see also Figure 7a). This is an example, at the highest resolution ever achieved in this region of Jupiter, of how filaments of red material are plucked from the GRS by an anticyclonic disturbance interacting with its edge in a similar way than the AVs. Nevertheless, the GRS velocity and vorticity maps (Figure 2) were similar to those reported for the 2012–2017 period (Sánchez-Lavega et al., 2018; Simon et al., 2018). The GRS showed a maximum averaged velocity $u_{\text{NS}} \sim 120 \text{ ms}^{-1}$ at the north and south edges of the red oval whereas the meridional

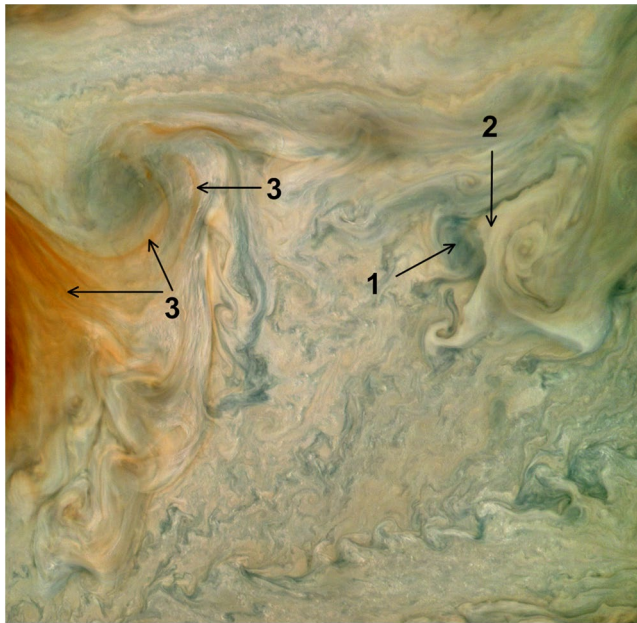


Figure 3. East side of the GRS observed by JunoCam on April 1, 2018 (see Figure 7 for context). The scene is chaotic with many eddies on different scales circulating the GRS southern flow. Most of them (greyish-brown ovals) look cyclonic, but there is a large anticyclonic eddy in contact with the east end of the GRS that is pulling red streamers around it. The map also shows aerosol layers at different altitudes according to their crossings and overlaps. At least three can be distinguished: (1) Deep gray features (undulating elongated filaments and oval vortices); (2) An extended white intermediate cloud with a variety of textures; (3) high orange-red clouds from the GRS edge and orange streamers. Comparing with the radiative transfer model (section 3.3), 1 and 2 could correspond to the upper cloud deck and 3 to the tropospheric haze. GRS, Great Red Spot.

peak velocities were smaller and different at the western ($v_W \sim 70 \text{ ms}^{-1}$) and eastern ($v_E \sim 110 \text{ ms}^{-1}$) sides (Figure 1d). The GRS flow had a ring of maximum relative vorticity with peak value $\zeta_r = 6 \times 10^{-5} \text{ s}^{-1}$, as reported in previous studies (Mitchell et al., 1981; Simon et al., 2018; Figure 2).

3.1. Phenomenology of the Interactions

The AV that interacted with the GRS appeared as whitish ovals surrounded by brownish rings (Figure 4). The high-resolution images of three of them show that the ring is not well defined but has irregular and fuzzy edges, and its clouds seem to reveal the background of clouds below them. The morphology of AV3 (Figure 4 bottom) exhibits a very diffuse outer ring, an inner ring of dark brown clouds, and the central whitish core with individual clouds inside it. The AVs were centered at planetographic latitude $\sim 20^\circ\text{S}$ – 21°S , had a characteristic size (as defined by the outer edge of the ring) of $\sim 5,000$ – $7,500 \text{ km}$ (east-west) by $3,000$ – $3,500 \text{ km}$ (north-south) and a core of $\sim 2,000 \text{ km}$, and moved westward (toward the GRS) at an absolute speed of $\sim 40 \text{ ms}^{-1}$, in agreement with the ambient wind profile (Figure 1c). When reaching the eastward edge of the GRS they were entrained by its anticyclonic flow, moving inside the northern collar (Figure 5a). Because the width of the hollow is similar to the size of AVs, they were compressed, stretched and fragmented (Figures 5b–5d), then skimming the outer edge of the red oval, they tore off material producing the streamers and flakes of red material that moved outward from the red oval (Figures 5e–5f). In some cases, the remnants from the AVs, along with the material that had been ripped off, fully circumnavigated the red oval, moving along the southern edge of the GRS and detaching from it at its east edge at latitude 25°S – 26°S . In other cases, they were expelled out of the GRS at its west edge. Additional examples of such interactions are shown in Figure 6. Descriptions, images and details of a large number of these events are given by Foster et al. (2020).

Figure 5g shows all the wind measurements performed between May 11 and 29, 2019 outside the red oval (i.e., along the GRS periphery and hollow) as derived from tracking the AV features, their fragments, and the streamers and flakes ripped from the red oval. We call streamers the long and narrow (thin) filaments (Figure 3), while the flakes are wide and irregular fragments of the GRS area (Figure 6), all of them mainly torn from the eastern and western edges of the GRS. Representative values of the drift velocity (in ms^{-1}) in the different sectors are given in the figure with velocity errors estimates ~ 5 – 10 ms^{-1} (section 2.1). During this period, the gap in the outer edge of the hollow at its northernmost point was closed, favoring the interactions by closing the alternative path of flow of the AVs out of the GRS hollow. Features interacting with the red oval edge moved at speeds up to 90 ms^{-1} . Upon interaction, the features slowed down rapidly in a short distance or even diluted and merged with clouds in the GRS hollow, thus disappearing. We have measured the probable deceleration of an AV fragment forming a flake from 93 ms^{-1} to 19 ms^{-1} followed by recovery of its speed to 90 ms^{-1} (Figures 5d–5f). As a consequence of these interactions the red oval showed important distortions from its elliptical shape (Figures 5d and 6). Detailed views of the GRS and its streamers and flakes in 2018–2019 can be seen in the high-resolution images occasionally obtained by JunoCam on board Juno (Figure 7).

3.2. Effects on the Dynamics of the GRS

The center of the red oval moved throughout 2019 with a mean drift in longitude of 0.33 deg/day in System III, equivalent to a zonal velocity $u = -4.5 \pm 0.2 \text{ ms}^{-1}$, with no drifts in latitude (Figure S1). Coupled to it, the well known regular 90-day oscillation in longitude (Solberg, 1969; Trigo-Rodríguez et al., 2000) persisted, but was perturbed increasing the oscillation to 125 days around days 620–640 (mid-May to early June 2019) and the amplitude A from 1° to 1.2° , although the oscillation showed no phase shift in the longer term

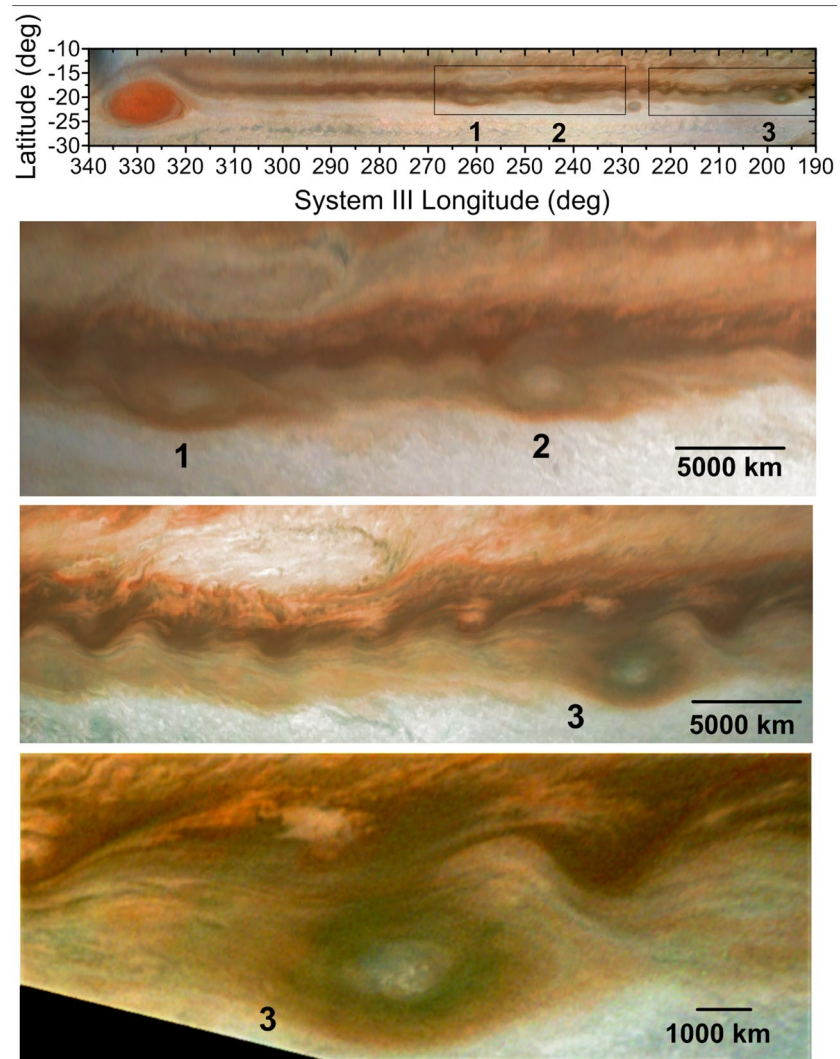


Figure 4. Examples of anticyclonic vortices (AV) or ring spots as imaged by JunoCam. This sequence was obtained during perijove 23 (PJ23) on November 3, 2019. The upper map shows the GRS and the selected AVs identified by numbers 1–3. The three lower maps are augmented versions to show the AV cloud morphology. The bottom map is a contrast-enhanced processed image of AV3 to show cloud details. GRS, Great Red Spot.

(Figure 8a, Figure S2). The most plausible explanation is that the AV interactions temporarily shifted the phase in the 90-day natural oscillation but preserved its maximum velocity $v_{\max} = A \omega 0.9 \text{ ms}^{-1}$ (A from 1° to 1.2° , frequency $\omega = 2\pi/\tau$ and τ the oscillation period, changing from 90 to 125 days during intense interactions). The shape and size of the red oval underwent noticeable changes during interactions (Figure 8b). The east-west length decreased from 15.5° (18,040 km) in early March 2019 to 13.7° (15,950 km) in May 2020. Large fluctuations occurred during the period of intense flake formation with the zonal length reaching a minimum value of 13° (15,130 km). Figure 8c shows the area changes of the red oval considering it as an ellipse with the strongest decrease in area of 25%.

We tracked the motions of well-contrasted dark features internal to the red oval (Figure 1) during intervals of ~ 1 –3 days in ground-based images in 2019 April–June and April 2020 to determine their velocities (Figures 5 and 6). Only the best measured 45 vectors were considered for which we estimate a 10% error in their velocity (Figure 8d). Among them there are 22 vectors in the red oval periphery that give a mean velocity $149 \pm 18 \text{ ms}^{-1}$, above the peak values of 120 ms^{-1} found on April 17, 2018 (Figure 1a) and in previous measurements (Sánchez-Lavega et al., 2018; Simon et al., 2018). Thus, the rotational velocity

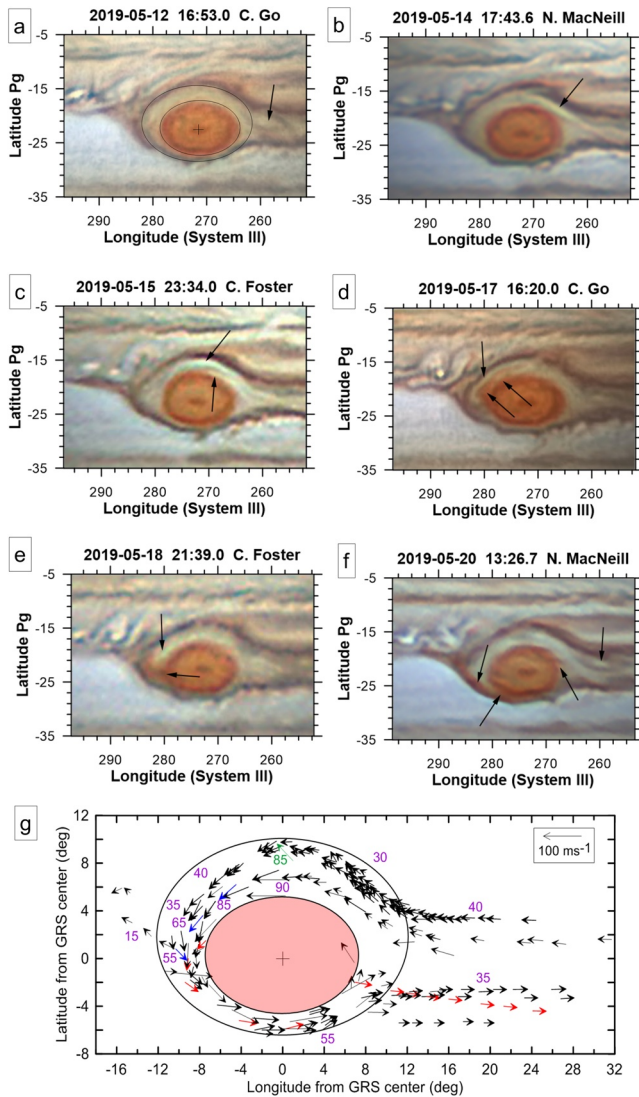


Figure 5. Interactions of anticyclones with the GRS (a–f) This sequence of mapped color-composite RGB images shows the full interaction of one AV with the GRS from May 10 to 20, 2019. The ellipse outlines (panel a) are drawn approximately as a reference. Dates, times and observers are identified in each panel. Arrows mark the location of the AV and its fragments and the flake formation on the west side of the GRS. Note that a new AV is entering the collar in (f). Other sequences of interactions are presented in Foster et al. (2020). (g) Wind vectors (in black) derived from cloud tracking from May 10 to June 10, 2019. The ellipses represent the red oval (red area) and outer periphery ring (open in the east edge). The red and blue vectors correspond to strong AV interactions and flake formation. Numbers (purple) give the value of the velocity in ms⁻¹. The green vector shows a particular velocity measured for an AV moving rapidly to the gap region on April 16, 2020. AV, anticyclonic vortices; GRS, Great Red Spot; RGB, red, green, and blue.

of the GRS accelerated following the AV interactions. However, the GRS maximum vorticity did not change. In 2018, it was $\zeta_V = 6.5 \times 10^{-5} \text{ s}^{-1}$ (Figure 2) and in 2019 we obtain $\zeta_V = 6.3 \times 10^{-5} \pm 1.2 \times 10^{-5} \text{ s}^{-1}$ using $\zeta_V \approx V_T \left[\frac{1}{b} \left(2 - \frac{e^2}{2} \right) \right]$ (Legarreta & Sánchez-Lavega, 2005) that assumes an elliptical shape for the GRS ($a = 5,700 \text{ km}$ and $b = 4,150 \text{ km}$ are the semi-major and semi-minor axis of the ellipse), $e = \sqrt{1 - \left(\frac{b}{a} \right)^2}$ is its eccentricity, and $V_T = 150 \text{ ms}^{-1}$ (data taken from Figure 8). These results are consistent with reported maximum velocities of 150 ms^{-1} and vorticity data from HST measurements in April and June 2019 (Wong et al., 2019).

3.3. Hazes and Cloud Models

We generated crude spectra in the wavelength range from 0.38 to $1.7 \mu\text{m}$ of the red oval, a flake and a reference white region using images obtained in May 27, 2019 with the PlanetCam astronomical camera (Mendikoa et al., 2016, 2017; Figures 9 and 10). The major differences between the GRS and the flake spectrum occur at short wavelengths where the reflectivity (I/F) of the flake is always higher than that of the GRS, while the reference region is brighter in the continuum and darker in the methane absorption bands. This spectral region is mainly sensitive to the particle number density and optical depth of the aerosol layers of the hazes. The description of the atmospheric parameters defining the aerosol vertical distribution in our radiative transfer model (see section 2.4) can be summarized as follows (Pérez-Hoyos et al., 2020): An uppermost stratospheric haze composed of small particles; an intermediate tropospheric haze of micron-sized particles that dominate the reflectivity measured in this work; and a bottom cloud with a limited effect on the modeling (Figures 10b and Table S3). While the uppermost and bottom aerosol layers were modeled with a single free parameter that accounts for the total optical thickness of the layer, the intermediate and most influential layer requires three free parameters for the vertical distribution (bottom pressure P_{bot} , peak particle density N and fractional scale height), two parameters to describe the particle size distribution (effective radius r_{eff} and dispersion σ) and the imaginary refractive index (mi) as a function of wavelength. The real refractive index was fixed to 1.43 at 890 nm and computed from the fitted imaginary values using the Kramers-Krönig relation as in Lucarini et al. (2005). Previous work has shown that this kind of model accounts well for the observed reflectivity at this spectral resolution in both Jupiter (Pérez-Hoyos et al., 2020) and Saturn (Sánchez-Lavega, Garcia-Melendo, et al., 2020; Sánchez-Lavega, Garcia-Munoz, et al., 2020).

The model that best fits the spectra (Figure 10, Table S3) consists of a thin upper stratospheric haze layer located at $P \sim 10 \text{ mbar}$ with similar properties in the GRS and flake. Below it, there is a tropospheric haze with base at $P \sim 200 \text{ mbar}$ and a deeper cloud deck with base at $P \sim 1 \text{ bar}$, consistent with previous studies (de Pater et al., 2010). It is in these two

aerosol layers where we find the differences between the GRS and the flake. The particle density and the optical depth in the tropospheric haze and upper cloud deck are about 50% lower in the flake area than in the GRS core. The GRS is brighter than the flake in the red spectral region (including the methane absorption bands) because of the higher particle density, but the altitude of these two layers is similar. On the other

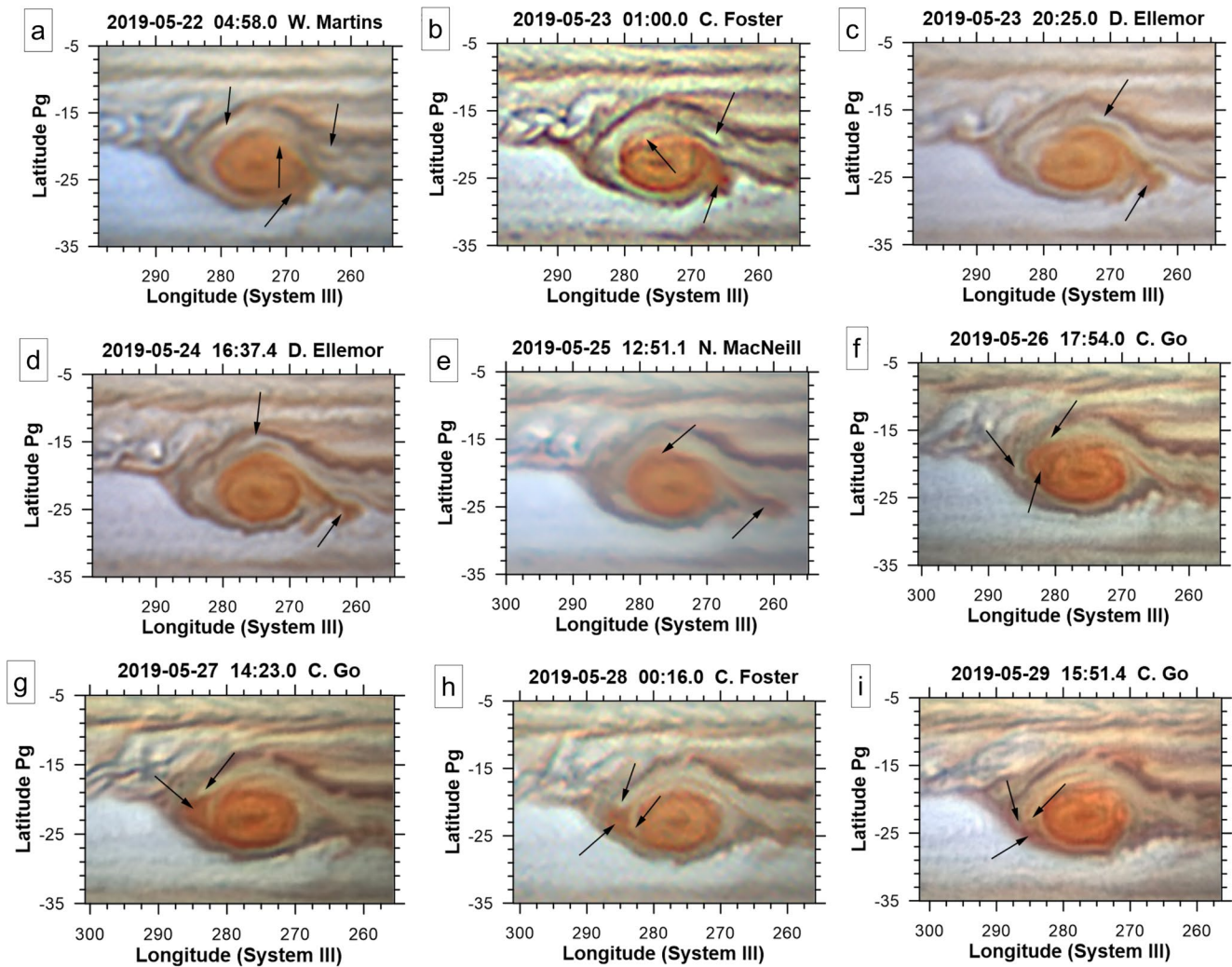


Figure 6. An AV interacting especially strongly with the GRS: A sequence of mapped color composite RGB images showing the interaction of an AV with the GRS from May 22 to 29, 2019. The date and observers are identified in each panel. The arrows mark the location of the AV and its fragments, the flake formation on the east side of the GRS, and a white cloud impinging on the GRS red oval. AV, anticyclonic vortices; GRS, Great Red Spot; RGB, red, green, and blue.

hand, the flake is brighter in the violet-blue spectral region than the GRS because of the lower absorption by the haze particles (lower imaginary refractive index, Figure 10c). The simplest explanation for this difference is that the flake haze and cloud have lower particle density than the red oval, being material that has been plucked and separated from it, probably containing some mixture of particles from the AV. The cloud morphology shown in JunoCam color images of the material outside the red oval supports this interpretation (Figures 1a, Figures 3, Figures 7a–7b). The thin layer of red aerosols spread and overcast the clouds below it. The optical depth of the flake is low enough to allow seeing the deeper clouds below it suggesting that the flakes are “a surface phenomenon” that essentially affects the aerosol particle density above the 1–2 bar pressure level.

4. Dynamical Interpretation

A large number of works describe 2-vortex and 3-vortex interactions, their distortions and shearing as in contour-dynamics studies (Legras & Dritschel, 1993), in applied-mathematics modeling (Tur & Yanovsky, 2017), as well as their phenomenology in natural systems and in laboratory in the presence of zonal jets (Galperin & Read, 2019). In this section, we use two types of numerical models, run under Jupiter

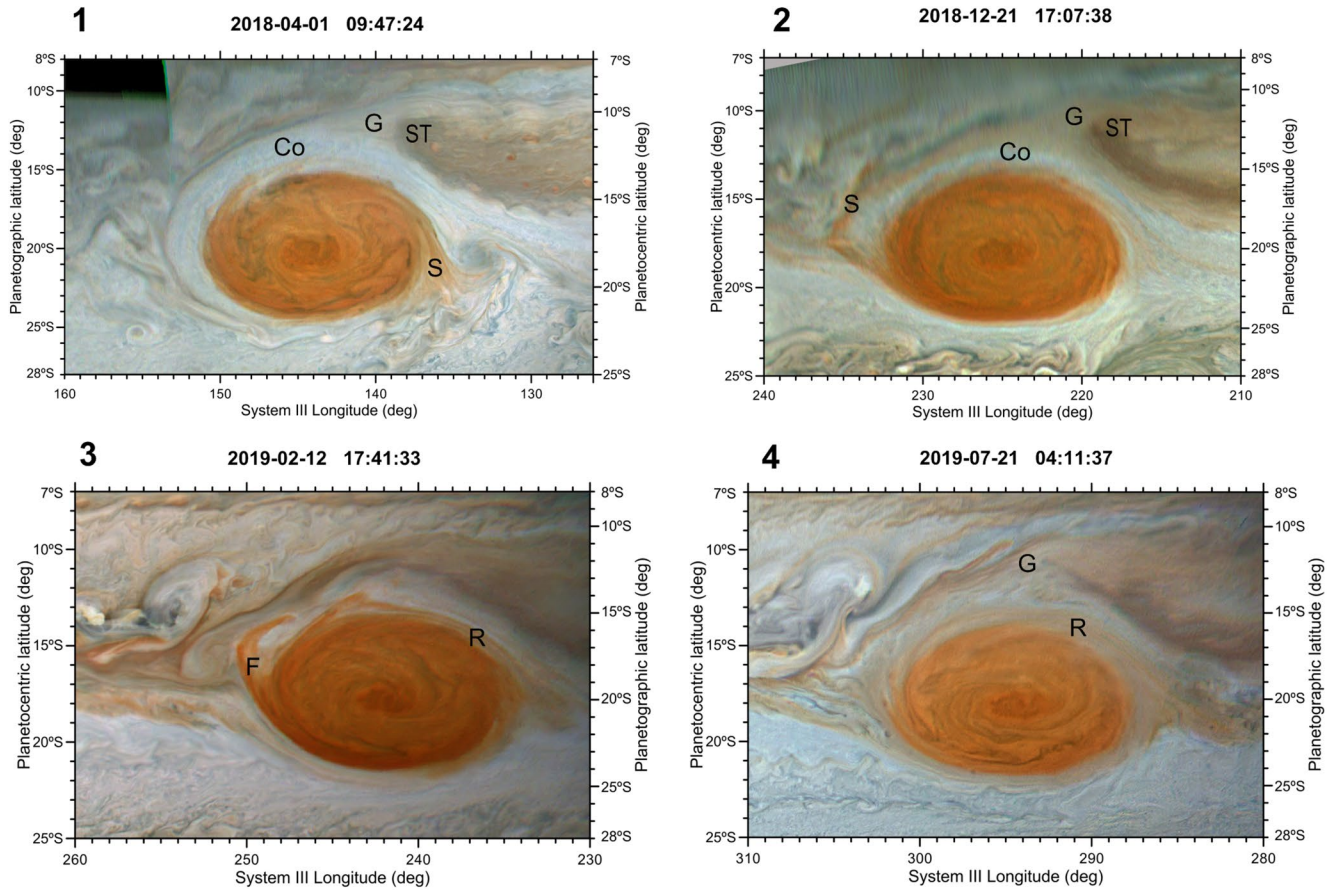


Figure 7. The GRS observed at high resolution by JunoCam. The maps correspond to the following dates: (1) Perijove PJ12 on April 1, 2018. Thin streamers are seen on the northwest and eastern sides (S) (see Figure 3). The gap (G) is open, the collar (Co) and the stagnation (ST) regions are well defined; (2) Perijove 17 (December 21, 2018). A large streamer (S) at the west edge with a width $\sim 1,250$ km is flowing away from the red area toward the hollow's outer edge. (3) Perijove 18 (February 12, 2019). A flake (F) has formed with white clouds between it and the red oval. A ring of reddish material (R) surrounds the east side of the red oval, probably due to a previous streamer or flake in this side. The gap is closed and the stagnation region is not defined. (4) Perijove 21 (July 21, 2019). This image was taken after the intense flake period in May–June 2019 and shows a ring of reddish material fully surrounding the red oval, probably due to the dispersion of the red chromophores from previous streamers and flakes. The gap is not well defined and apparently appears to be closed since the stagnation region is also not evident. GRS, Great Red Spot.

conditions, to address to address the observed interactions and explore their dependence with the vortices properties.

4.1. Numerical Simulations of the Dynamics of the Interaction

We have used a shallow water model SW (García-Melendo & Sánchez-Lavega, 2017) and the explicit planetary isentropic-coordinate (EPIC) multi-layer model (Dowling et al., 1998) to simulate the dynamics of the interaction between the GRS and an AV. The SW model is fast, retains a good deal of the large scale atmospheric physics and is justified for interactions between vortices with horizontal size \gg vertical extent (Sánchez-Lavega, Garcia-Melendo, et al., 2020). The EPIC model allows one to incorporate the vertical structure of the atmosphere and the altitude and vertical extent of the interacting vortices. The dynamic field is represented in both models by the Potential Vorticity, which acts as a material tracer of the flow.

$PV = \frac{f + \zeta_V}{h}$ for the SW model and $PV = \frac{(f + \zeta_V)}{\rho} \left(\frac{\partial \theta}{\partial z} \right)$ for the EPIC model, where h is the layer thickness, ρ is the density, θ is the potential temperature, z the vertical coordinate, and $f = 2\Omega \sin \varphi$ the Coriolis parameter (Ω is Jupiter's angular velocity, φ the latitude; Sánchez-Lavega, 2011). In both models, we introduce two vortices, with horizontal size and velocity at periphery in the range of those of the GRS and AV respectively, into Jupiter's background wind velocity profile at their corresponding latitudes (Table S4).

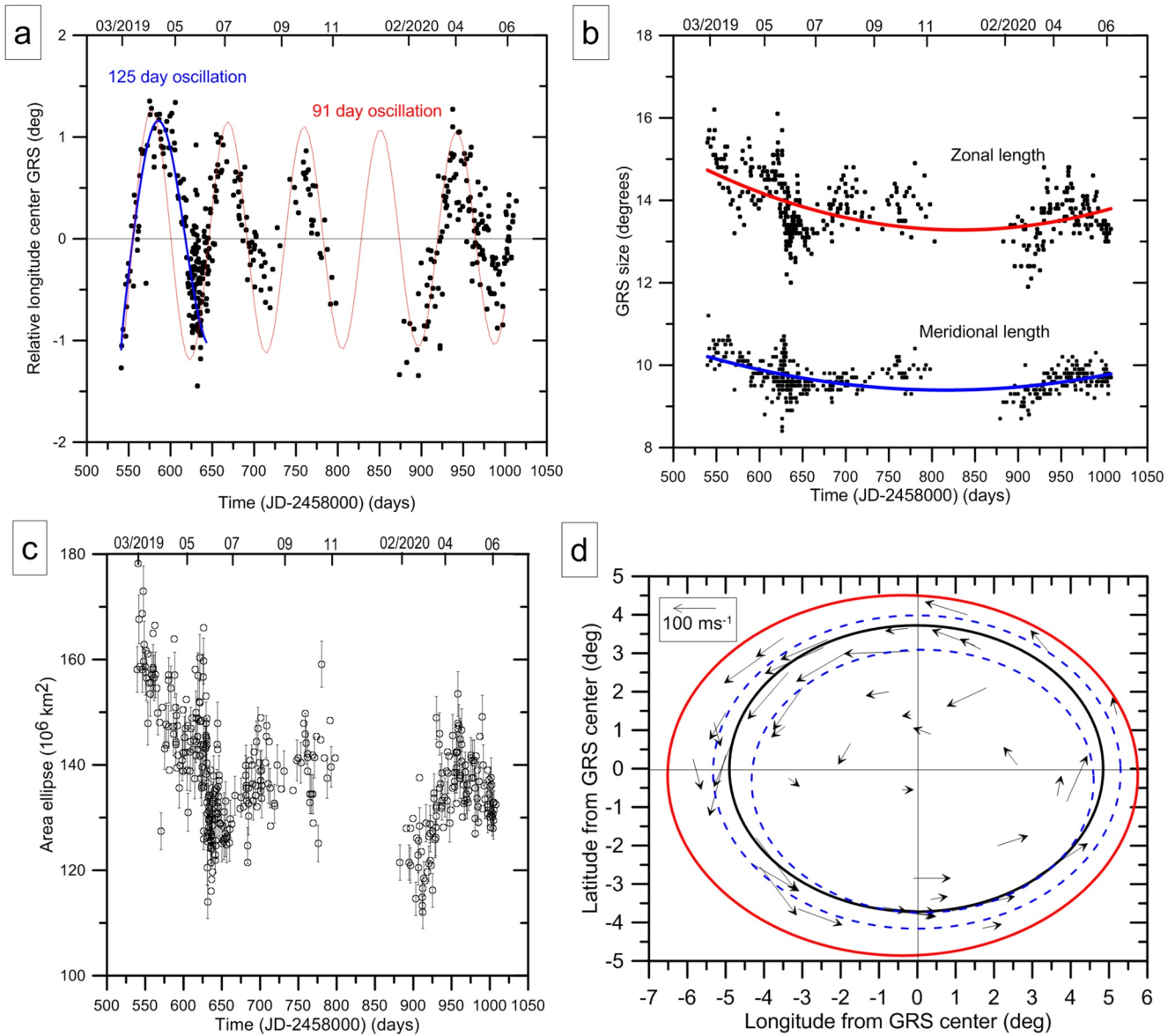


Figure 8. Effects of the interactions on the GRS dynamics. (a) Oscillations in longitude of the center of the GRS relative to its mean drift (Figure S1) and fits to a sinusoidal function with different periods and amplitudes. Bottom x-axis shows time Julian Date, while the corresponding month (start date) and year indicated at the top. (b) Zonal length (major axis) and meridional width (minor axis) of the GRS red oval area during the observing period. Typical errors in the size measurements range from $\pm 0.5^\circ$ to $\pm 1^\circ$ depending on image quality. The red and blue curves show second-degree polynomial fits. (c) Area of the red ellipse from measurements in (b). Large fluctuations are seen in May–July 2019 (JD \sim 2458600–2458700) with strongest area decrease between JD \sim 2458550–2458625 (March 7 to May 21, 2019). (d) Wind vectors from tracking the motions of distinct features in the GRS interior in April–June 2019 and in April 2020. Typical errors in the velocity measurements are $\sim 10 \text{ ms}^{-1}$. The black line shows the approximate best-fitting ellipse where velocity has a maximum, with uncertainty roughly indicated by the ellipses in dashed blue lines. The red line represents the edge of the red oval at the epoch of strongest interactions. GRS, Great Red Spot.

A parallel version of the Shallow Water model (Sánchez-Lavega, García-Melendo, et al., 2020; Soria et al., 2020) was run at the Mare Nostrum 4 supercomputer hosted at the Barcelona Supercomputing Center. Jupiter’s zonal winds were continuously forced (García-Melendo and Sánchez-Lavega., 2017). Grid resolution was 0.025° per volume control and time step size was 1 s, which ensured that the Courant-Friedrichs-Lewy condition was never violated. In our model, the barotropic Rossby radius of deformation is given by $L_R = (gH_0)^{1/2}/f \sim 1,200 \text{ km}$ for gravity acceleration $g = 25 \text{ ms}^{-2}$, undisturbed layer depth $H_0 = 1,000 \text{ m}$, and Coriolis parameter $f = 1.31 \times 10^{-14} \text{ s}^{-1}$. The simulation domain was a channel with periodic conditions in longitude, full slip on the latitude limits, and a flat bottom. Both vortices, the GRS and AV, were initially

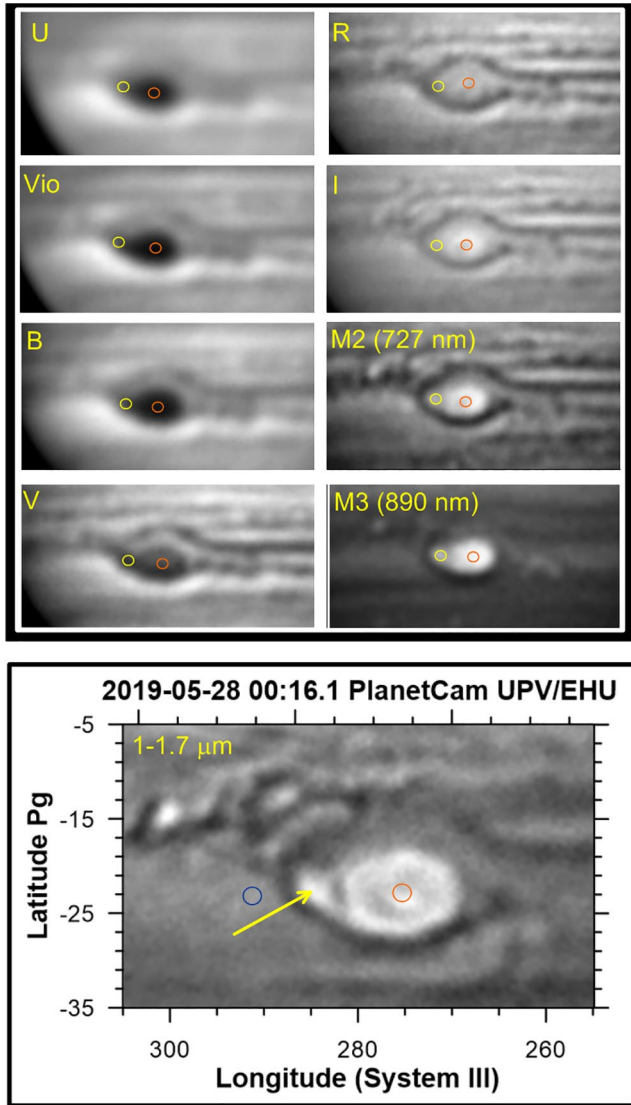


Figure 9. The GRS and a flake imaged at different wavelengths. Images obtained on May 28, 2019 with different filters (identified by their symbol) using Planetcam astronomical camera mounted at the 2.2 m telescope at Calar Alto Observatory (Mendikoa et al., 2016, 2017). The flake is shown at the western edge of the GRS and is marked by a yellow circle and an arrow in the last image. The photometric area in the center of the GRS is marked with an orange circle. The reference area is marked with a blue circle. These images have been contrast-enhanced to sharpen details but their photometric versions employed in the radiative transfer analysis were unprocessed. GRS, Great Red Spot.

introduced in geostrophic equilibrium. SW equations allowed fully explicit numerical schemes which allowed a very efficient parallelization by using a domain-decomposition strategy. The range of values of the parameters used in the simulations are given in Table S4A.

In Figure 11a we show the result of the SW simulations for the case of a strong interaction when AV has a tangential velocity at periphery $V_T = 100 \text{ ms}^{-1}$. In such a case, the AV impinges on the GRS southern flank, and as a consequence it stretches and lengthens, distorting the GRS oval shape and generating a large flake at its western side from material detached from the red oval. This case simulates very well the formation of the flakes (compare the western features with Figures 5–7). For weaker interactions when AV has $V_T \sim 50\text{--}60 \text{ ms}^{-1}$, streamers and flakes also form but they are less prominent and the AV material does not penetrate the GRS. Penetration of the AV into the GRS and the formation of flakes instead of streamers, occur preferably when $V_T \geq \sim 100 \text{ ms}^{-1}$ (Figure S4).

The EPIC model allows simulating interactions for different vertical extensions of the GRS and AV. The penetration depth of the PV anomaly for an axisymmetric vortex in hydrostatic and gradient-wind balance, like the GRS (Sánchez-Lavega et al., 2018), is given by (Wang et al., 1996)

$$D = \frac{L}{N} [(f + \zeta_V)(f + \zeta_{\text{amb}})]^{1/2}. \quad (1)$$

Taking a Brunt-Väisälä frequency in the range $N \sim 1$ to $5 \times 10^{-3} \text{ s}^{-1}$ (de Pater et al., 2010), ambient vorticity (meridional shear of the zonal wind) $\zeta_{\text{amb}} \approx \frac{\partial u}{\partial y} = 1.16 \times 10^{-5} \text{ s}^{-1}$ and horizontal scale of the flow $L \sim 9,000 \text{ km}$ (peak to peak meridional distance in the zonal wind maxima north and south of the GRS; Figure 1), $f = -1.25 \times 10^{-4} \text{ s}^{-1}$ and GRS vorticity $\zeta_V = 6.5 \times 10^{-5} \text{ s}^{-1}$, we get $D_{\text{GRS}} \sim 290\text{--}1450 \text{ km}$. This range of values is consistent with the retrievals of the GRS depth derived from radiances obtained with Juno’s infrared MWR experiment (Li et al., 2017) and from the study of the gravity field anomalies (Galanti et al., 2019; Galanti et al., 2019) that indicate that the GRS extends at least down to the 240 bars level (or about 350 km below the ammonia upper cloud at 1 bar). In recent anticyclone modeling and laboratory work, Lemasquerier et al. (2020) deduced that the GRS would have a depth of $150 \text{ km}^{+104}_{-56} \text{ km}$, less than indicated above. This determination strongly depends on the stratification N , as Equation 1 requires $N = 0.01 \text{ s}^{-1}$ to get 150 km. Given the high uncertainty in the value of N , we think that the range of values (290–1450 km) calculated above is more plausible. We tested different vertical extents for the GRS ($D_{\text{GRS}} \sim 200\text{--}300 \text{ km}$) centered at 0.68 bar level. We then applied a simple scale ratio between the horizontal size and depth for the vortices to take $D_{\text{AV}} \sim 0.1\text{--}0.3 D_{\text{GRS}}$ in agreement with previous studies (de Pater et al., 2010).

For the EPIC simulations we define the structure of the atmosphere as shown in Figure S3 for a variety of situations and with the model parameters for Jupiter as defined in Morales-Juberías et al. (2003) and García-Melendo et al. (2009) with the tested range of values given in Table S4B. For the small anticyclones AV we do not have measurements of the velocity at the periphery (rotation speed) and we estimate the range of values to use in the simulations assuming the vortex is in geostrophic balance with Rossby number in the range $Ro \sim V_T/fL \sim 0.07\text{--}0.15$ that follows our previous observations and models of Jovian anticyclones (Legarreta & Sánchez-Lavega, 2005). Here L is the vortex size and f the Coriolis parameter that leads to tangential velocities $V_T (\text{AV})_{\text{max}} = 50\text{--}120 \text{ ms}^{-1}$.

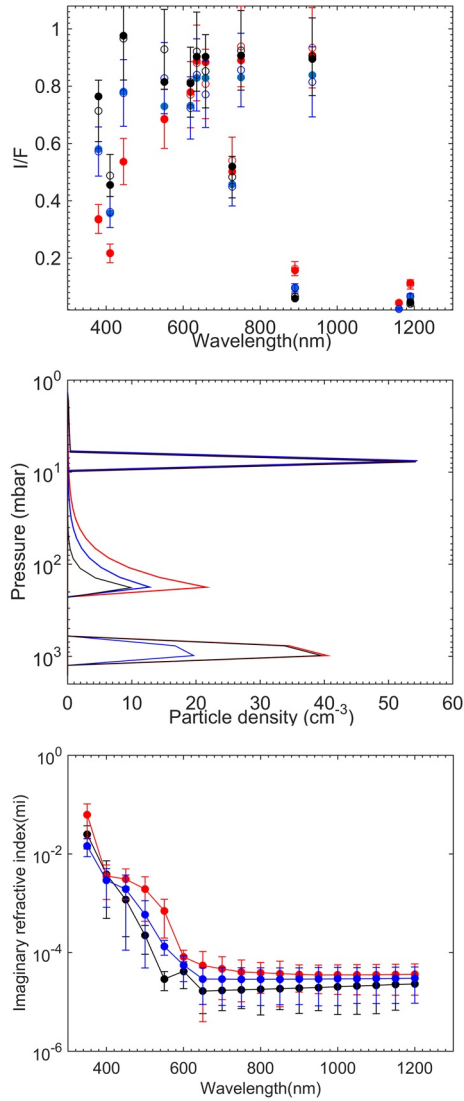


Figure 10. Photometry and radiative transfer model of aerosol vertical distribution. (a) Absolute reflectivity (I/F) spectra of the center of the GRS red core (red dots), a flake area (blue dots) and a reference region (black dots) obtained in May 27, 2019. The circles are the best model fits to the data; (b) The particle density as a function of altitude in the GRS (red), flake area (blue) and a reference region (black) according to a radiative transfer model; (c) Refractive imaginary index of the tropospheric haze particles using the same color code as in (b) (details given in Table S3). GRS, Great Red Spot.

In Figure 11b we show results from the EPIC simulations for an intermediate case in which the GRS has twice the speed at its periphery than the AV and its vertical extent is three times that of it. This case shows that as the interaction of the AV with the northern edge of the GRS progresses, the AV vortex lengthens while penetrating the GRS, strongly distorting its shape. The stretched AV becomes fragmented, being dragged by the circulation of the GRS where it generates a wave disturbance at the periphery of the red oval (Figure S5). This disturbance circulates through the external part of the GRS while the elongated AV along with part of the red oval material separates on its west side from it. Both the SW and EPIC model simulations form streamers and flakes. The SW model constrains the configurations in the horizontal plane (vortices location in latitude, relative velocities, relative sizes and intensities) in which the type of observed interaction occurs. The EPIC model confirms these values and strongly indicates that flake and streamer formation is a “surface” phenomenon mainly occurring in the upper cloud layers of the GRS.

4.2. GRS Internal Energy Change

An AV that is totally absorbed by the GRS adds energy (per unit mass) due to its own rotation, $E_{rot} \approx (1/2)V_{rot}^2 \sim 1250 \text{ Jkg}^{-1}$, and its velocity, $E_k \approx (1/2)u^2 \sim 800 \text{ Jkg}^{-1}$ ($V_r = 100 \text{ ms}^{-1}$, $u = 40 \text{ ms}^{-1}$ relative to GRS; Figure 5). If this energy is totally converted into heat during the frictional and mixing processes, the temperature must increase in the outer part of the GRS where the vortex is absorbed by $\Delta T \approx (E_{rot} + E_k) / C_p \sim 0.2 \text{ K}$, where $C_p = 12,360 \text{ JKg}^{-1}\text{K}^{-1}$, the specific heat at constant pressure. This is an upper value since the energy losses, e.g., radiative, have not been considered. The added energy will increase the radial temperature gradient $(dT/dr)_p$ in the GRS interior and assuming the vortex is under gradient wind balance (Mitchell et al., 1981; Sánchez-Lavega et al., 2018), we can estimate the change in its rotational velocity from the use of the thermal wind balance (Flasar et al., 1981; Fletcher et al., 2010; Pérez-Hoyos et al., 2009),

$$\frac{\partial V_r}{\partial \ln P} = -\frac{R_g^*}{(f + \zeta_V)} \left(\frac{\partial T}{\partial r} \right)_p \quad (2)$$

We take the wind measurements at a pressure level $P = 600 \text{ mbar}$ and we assume null speed at 20 mbar (Conrath et al., 1981) both before and after the interactions. The altitude difference between these two levels is $\ln(600/20) = 3.4$ scale heights, and taking $(f + \zeta_V) \sim -6.5 \times 10^{-5} \text{ s}^{-1}$ (in 2018 and 2019), $R_g^* = 3,750 \text{ JKg}^{-1}\text{K}^{-1}$. From Equation 2 we get an average horizontal temperature gradient of $(\partial T / \partial r)_p = -6.5 \times 10^{-4} \text{ Kkm}^{-1}$ in 2018 and $-7.75 \times 10^{-4} \text{ Kkm}^{-1}$ in 2019. We then calculate temperature difference between the GRS center and the collar with peak vorticity (average distance r) using that gradient at the semi-major axis and semi-minor axis of the ellipse that defines the collar of maximum vorticity ($a = 4,420 \text{ km}$, $b = 2805 \text{ km}$ in 2018 from Figure 2; $a = 5,000\text{--}5,700 \text{ km}$, $b = 3,500\text{--}4,150 \text{ km}$ in 2019 from ellipses traced in Figure 8d). This gives $\Delta T \approx -\left(\frac{\partial T}{\partial r}\right)_p r \sim 2.2 \text{ K}$ ($\Delta T = 2.6$ and 1.7 K at (a) and (b) to have $V_r(\text{max}) = 120 \text{ ms}^{-1}$ (in 2018)), and $\Delta T \sim 3.3\text{--}3.8 \text{ K}$ ($\Delta T = 3.9\text{--}4.4 \text{ K}$ and $2.7\text{--}3.2 \text{ K}$ at (a) and (b) to have $V_r(\text{max}) = 150 \text{ ms}^{-1}$ (in 2019)). These rough numbers agree with previously measured temperature contrasts in the GRS (Fletcher et al., 2010). The deposited energy from AVs is multiplicative with the number of vortices interacting with the GRS, which was only 0.17 per month averaged from 2016 March to 2018 June, but 2.0 per month averaged from 2019 March to June. Thus, a moderate

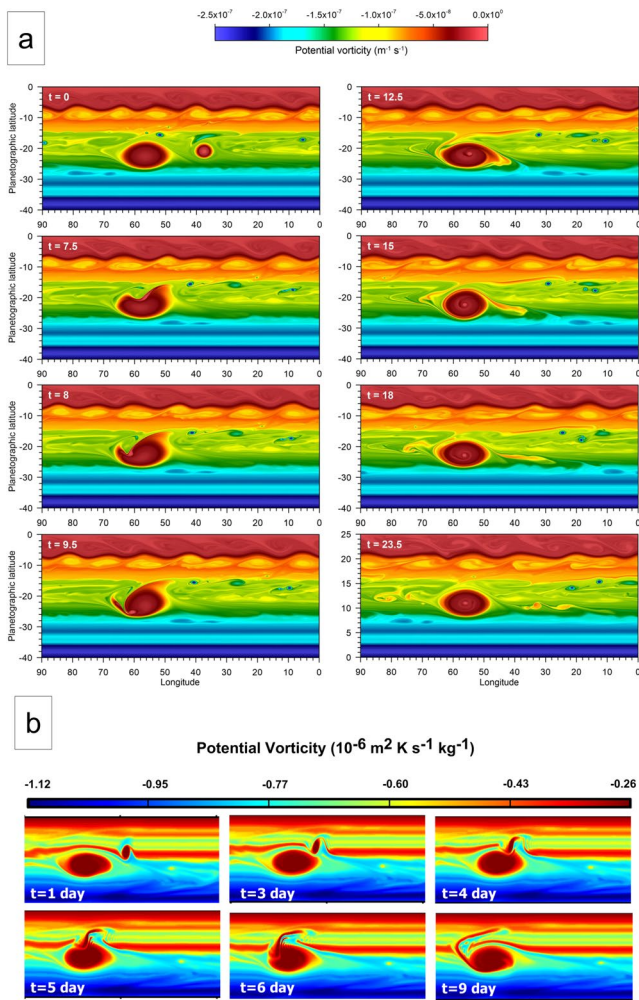


Figure 11. Numerical simulations of the interactions of the GRS and an AV. Potential Vorticity maps for two type of models: (a) SW simulations of the interaction for the GRS and an AV at latitude 20.0°S , both with peak tangential velocity $V_T = 100 \text{ ms}^{-1}$. Time (t) is given in days. (b) EPIC simulations with $V_T = 100 \text{ ms}^{-1}$ (GRS) and $V_T = 50 \text{ ms}^{-1}$ (AV), with a vertical extent of 6 scale heights ($\sim 120 \text{ km}$) for GRS and 2 scale heights ($\sim 40 \text{ km}$) for AV, with both vortices centered at pressure level $P = 680 \text{ mbar}$. Other data are given in Table S4. AV, anticyclonic vortices; EPIC, explicit planetary isentropic-coordinate; GRS, Great Red Spot

heating due to energy absorption provided by the AVs as calculated above could produce the observed increase in the peak tangential velocity at cloud tops.

5. Discussion and Conclusions

In 2018–2020, Jupiter’s GRS long lifetime survival appeared to be threatened following strong interactions with series of smaller AV, giving rise to the following events:

- The GRS increased its maximum tangential velocity up to 150 ms^{-1} .
- The GRS vorticity did not change.
- The visible red area decreased when the AVs tore off large fragments and distorted its shape.
- The GRS suffered a transient change in its steady 90-day oscillation in longitude, increasing its period and amplitude.

From a radiative transfer analysis of the GRS reflectivity in the visual and near-infrared wavelengths we have shown that the interactions affected the upper cloud tops of the GRS. This is also confirmed by numerical simulations of the dynamics of these interactions using a shallow water model and a general circulation model.

Encounters between anticyclones of similar size lead to complete mergers (Mac Low & Ingersoll, 1986), as was the case of the large and long-lived three White Ovals that 20 years ago generated a single steady anticyclone BA (length $\sim 11,000 \text{ km}$, about half the GRS current size) (Sánchez-Lavega et al., 1999, 2001) with a similar velocity field to its predecessors and to the GRS (Hueso et al., 2009). However, the GRS interactions behave differently since it is a single large anticyclone at its latitude. The GRS has been slowly decreasing in size since the late nineteenth century (Rogers, 1995; Simon et al., 2018), and in 2019 the interactions with AVs reduced the visible red oval to the smallest size ever recorded while increasing peak velocities but preserving its vorticity (within the precision of ground-based measurements). The flaking events are likely to have been superficial, not affecting the full depth of the GRS. Indeed, by October 2019, the visible red oval had almost recovered to its previous size (Figure 8c). Our analysis confirms that the ingestion of AVs is not necessarily destructive (Vasavada & Showman, 2005); it can increase the GRS wind speed, and perhaps over a longer period, maintain it in a steady state (Dowling et al., 1989; Sada et al., 1996). The intense vorticity of the GRS, together with its larger size and depth, compared to the interacting vortices, guarantees its long lifetime.

Data Availability Statement

Sánchez-Lavega, (2021): Jupiter Great Red Spot flakes. figshare. Collection. <https://doi.org/10.6084/m9.figshare.c.5226206.v2>

The ground-based images included in the above repository have been downloaded from the following sources:

Association of Lunar and Planetary Observers ALPO – Japan: <http://alpo-j.sakura.ne.jp/Latest/Jupiter.htm>

PVOL2 database: <http://pvol2.ehu.eus/pvol2/>

Images from the HST-OPAL program are available at: <https://archive.stsci.edu/prepds/opal/>

Juno/Junocam images are available at NASA PDS (Planetary Data System): <https://pds-imaging.jpl.nasa.gov/data/juno/>

The image navigation software WinJupos is available at: <http://jupos.org/gh/download.htm>

Hueso (2020). Particle Image Correlation Velocimetry Software PICV3: <http://doi.org/10.5281/zenodo.4312675>

Irwin, P (2020). NEMESIS/Radiative transfer code software: <https://doi.org/10.5281/zenodo.4303976>

Soria, M., García-Melendo, E., Prat, A (2020). Shallow Water Model, Shallow Worlds 2. <https://doi.org/10.5281/zenodo.4312681>

The EPIC numerical model is an open-code funded by NASA, available in the Atmospheres Node of the PDS: https://atmos.nmsu.edu/data_and_services/software/epic/epic.htm

Acknowledgments

This work has been supported by the Spanish project AYA2015-65041-P and PID2019-109467GB-I00 (MINECO/FEDER, UE) and Grupos Gobierno Vasco IT1366-19. PI acknowledges a PhD scholarship from Gobierno Vasco. EGM is Serra Hunter Fellow at UPC. This work used data acquired from the NASA/ESA HST Space Telescope, associated with OPAL program (PI: Simon, G013937), and archived by the Space Telescope Science Institute, which is operated by the Association of Universities for Research in Astronomy, Inc., under NASA contract NAS 5-26,555. All maps are available at <http://dx.doi.org/10.17909/T9G593>. PlanetCam observations were collected at the Centro Astronómico Hispánico en Andalucía (CAHA), operated jointly by the Instituto de Astrofísica de Andalucía (CSIC) and the Andalusian Universities (Junta de Andalucía). EGM, MS, APG, MAC and ASL thankfully acknowledge the computer resources at Mare Nostrum and the technical support provided by Barcelona Supercomputing Center (AECT-2019-2-0006). This research has made use of the USGS Integrated Software for Imagers and Spectrometers (ISIS). We appreciate the contribution from all observers cited in Table S1 for his fundamental contribution to this study with Jupiter images obtained with high dedication and skill. GSO and TM were supported by NASA with funds distributed to the Jet Propulsion Laboratory, California Institute of Technology.

References

Acton, C. H. (2016). Ancillary data services of NASA's Navigation and Ancillary Information Facility. *Planetary and Space Science*, 44, 65–70. [https://doi.org/10.1016/0032-0633\(95\)00107-7](https://doi.org/10.1016/0032-0633(95)00107-7)

Caplinger, M. (2016). Malin Space Science Systems Inc. In *Juno, software interface specification, JunoCam standard data products version 1.3*. Available at NASA PDS. Retrieved from https://pds-imaging.jpl.nasa.gov/data/juno/JNOJNC_0001/DOCUMENT/JUNO_JNC_EDR_RDR_DPSIS.PDF

Conrath, B. J., Flasar, F. M., & Pirraglia, J. A. (1981). Thermal structure and dynamics of the Jovian atmosphere 2. Visible cloud features. *Journal of Geophysical Research*, 86, 8769–8775. <https://doi.org/10.1029/JA086iA10p08769>

de Pater, I., Wong, M. H., Marcus, P., Luszcz-Cook, S., Ádámkóvics, M., Conrad, A., et al. (2010). Persistent rings in and around Jupiter's anticyclones – Observations and theory. *Icarus*, 210(2), 742–762. <https://doi.org/10.1016/j.icarus.2010.07.027>

Dowling, T. E., Fisher, A. S., Gierasch, P. J., Harrington, J., LeBeau, R. P., & Santori, C. M. (1998). The explicit planetary isentropic-coordinate (EPIC) atmospheric model. *Icarus*, 132, 221–238. <https://doi.org/10.1006/icar.1998.5917>

Dowling, T. E., & Ingersoll, A. P. (1989). Jupiter's Great Red Spot as a Shallow Water System. *Journal of the Atmospheric Sciences*, 46, 3256–3278. [https://doi.org/10.1175/1520-0469\(1989\)046%3C3256:JGRSAA%3E2.0.CO;2](https://doi.org/10.1175/1520-0469(1989)046%3C3256:JGRSAA%3E2.0.CO;2)

Flasar, F. M., Conrath, B. J., Pirraglia, J. A., Clark, P. C., French, R. G., & Gierasch, P. J. (1981). Thermal Structure and Dynamics of the Jovian Atmosphere 1. The Great Red Spot. *Journal of Geophysical Research*, 86, 8759–8767. <https://doi.org/10.1029/JA086iA10p08759>

Fletcher, L. N., Orton, G. S., Mousis, O., Yanamandra-Fisher, P., Parrish, P. D., Irwin, P. G. J., et al. (2010). Thermal structure and composition of Jupiter's Great Red Spot from high-resolution thermal imaging. *Icarus*, 208, 306–328. <https://doi.org/10.1016/j.icarus.2010.01.005>

Foster, C., Rogers, J. H., Mizumoto, S., Casely, A., & Vedovato, M. (2020). *Jupiter in 2019 Report no.10: The GRS in 2019 and its interaction with retrograding vortices as monitored by the amateur planetary imaging community*. British Astronomical Association. Retrieved from <https://britastro.org/node/22552>

Galanti, E., Kaspi, Y., Parisi, M., Folkner, W. M., Durante, D., Simons, F. J., & Bolton, S. J. (2019). How deep is the Great Red Spot? A multimethod analysis using the recent Juno gravity. *Measurements, EPSC-DPS Joint Meeting, EPSC Abstracts*, 13. EPSC-DPS2019-1228-1.

Galperin, B., & Read, P. (2019). *Zonal jets, phenomenology, genesis and physics*. Cambridge, UK. Cambridge University Press.

García-Melendo, E., Legarreta, J., Sánchez-Lavega, A., Hueso, R., Pérez-Hoyos, S., González, J., & Gómez-Forrellad, J. M., & IOPW Team. (2009). The jovian anticyclone BA: I. Motions and interaction with the GRS from observations and non-linear simulations. *Icarus*, 203, 486–498. <https://doi.org/10.1016/j.icarus.2009.05.031>

García-Melendo, E. & Sánchez-Lavega, A. (2017). Shallow Water simulations of Saturn's Giant Storms at different latitudes. *Icarus*, 286, 241–260. <https://doi.org/10.1016/j.icarus.2016.10.006>

GDAL/OGR contributors. (2020). *GDAL/OGR geospatial data abstraction software library*. Open Source Geospatial Foundation. Retrieved from <http://www.gdal.org/>

Hueso, R. (2020). *Particle image correlation Velocimetry software PICV3*. Zenodo. <http://doi.org/10.5281/zenodo.4312675>

Hueso, R., Juaristi, J., Legarreta, J., Sánchez-Lavega, A., Rojas, J. F., Erard, S., et al. (2018). The Planetary Virtual Observatory and Laboratory (PVOL) and its integration into the Virtual European Solar and Planetary Access (VESPA). *Planetary and Space Science*, 150, 22–35. <https://doi.org/10.1016/j.pss.2017.03.014>

Hueso, R., Legarreta, J., García-Melendo, E., Sánchez-Lavega, A., & Pérez-Hoyos, S. (2009). The Jovian anticyclone BA: II. Circulation and models of its interaction with the zonal jets. *Icarus*, 203, 499–515. <https://doi.org/10.1016/j.icarus.2009.05.004>

Irwin, P. (2020). *NEMESIS/Radiative transfer code software*. Zenodo. <https://doi.org/10.5281/zenodo.4303976>

Irwin, P. G. J., Teanby, N. A., de Kok, R., Fletcher, L. N., Howett, C. J. A., Tsang, C. C. C., et al. (2008). The NEMESIS planetary atmosphere radiative transfer and retrieval tool. *Journal of Quantitative Spectroscopy and Radiative Transfer*, 109, 1136–1150. <https://doi.org/10.1016/j.jqsrt.2007.11.006>

Karkoschka, E., & Tomasko, M. G. (2010). Methane absorption coefficients for the Jovian planets from laboratory, Huygens, and HST data. *Icarus*, 205, 674–694. <https://doi.org/10.1016/j.icarus.2009.07.044>

Legarreta, J., & Sánchez-Lavega, A. (2005). Jupiter's cyclones and anticyclones vorticity from Voyager and Galileo images. *Icarus*, 174, 178–191. <https://doi.org/10.1016/j.icarus.2004.10.006>

Legras, B., & Dritschel, D. (1993). *Vortex Stripping and the Generation of High Vorticity Gradients in Two-Dimensional Flows*. In F. T. M., Nieuwstadt, (Eds.). *Advances in turbulence IV. Fluid mechanics and its applications*. Springer, Vol. 18. https://doi.org/10.1007/978-94-011-1689-3_70

Lemasquerier, D., Facchini, G., Favier, B., Le Bars, M. (2020). Remote determination of the shape of Jupiter's vortices from laboratory experiments. *Nature Physics*, 16, 695–700. <https://doi.org/10.1038/s41567-020-0833-9>

Li, C., Oyafuso, F. A., Brown, S. T., Atreya, S. K., Orton, G. S., Ingersoll, A. P., & Janssen, M. A. (2017). *How Deep is Jupiter's Great red spot?* Paper Presented at American Geophysical Union Fall Meeting 2017. New Orleans, LA. American Geophysical Union. [http://refhub.elsevier.com/S0032-0633\(19\)30059-5/sref23](http://refhub.elsevier.com/S0032-0633(19)30059-5/sref23)

- Li, L., Ingersoll, A. P., Vasavada, A. R., Porco, C. C., Del Genio, A. D., & Ewald, S. P. (2004). Life cycles of spots on Jupiter from Cassini images. *Icarus*, *172*(1), 9–23. <https://doi.org/10.1016/j.icarus.2003.10.015>
- Lucarini, V., Saarinen, J. J., Peiponen, K. E., & Vartiainen, E. M. (2005). *Kramers–krönig relations in optical materials research*. Germany: Springer-Verlag Berlin Heidelberg. <https://doi.org/10.1007/b138913>
- Mac Low, M., & Ingersoll, A. P. (1986). Merging of vortices in the atmosphere of Jupiter: An analysis of Voyager images. *Icarus*, *65*, 353–369. [https://doi.org/10.1016/0019-1035\(86\)90143-0](https://doi.org/10.1016/0019-1035(86)90143-0)
- Mendikoa, I., Sánchez-Lavega, A., Pérez-Hoyos, S., Hueso, R., Rojas, J. F., Aceituno, J., et al. (2016). PlanetCam UPV/EHU: A two channel lucky imaging camera for Solar System studies in the spectral range 0.38–1.7 μm . *Pub. Astron. Soc. Pacific*, *128*, 035002. <https://doi.org/10.1088/1538-3873/128/961/035002>
- Mendikoa, I., Sánchez-Lavega, A., Pérez-Hoyos, S., Hueso, R., Rojas, J. F., & López-Santiago, J. (2017). Temporal and spatial variations of Jupiter's and Saturn's absolute reflectivity from 0.38 to 1.7 μm using PlanetCam-UPV/EHU. *Astronomy & Astrophysics*, *607*, A72. <https://doi.org/10.1051/0004-6361/201731109>
- Mitchell, J. L., Beebe, R. F., Ingersoll, A. P., & Garneau, G. W. (1981). Flow fields within Jupiter's great red spot and white oval BC. *Journal of Geophysical Research*, *86*, 8751–8757. <https://doi.org/10.1029/JA086iA10p08751>
- Morales-Juberías, R., Sánchez-Lavega, A., & Dowling, T. (2003). EPIC simulations of the merger of Jupiter's White Ovals BE and FA: Altitude dependent behavior. *Icarus*, *166*, 63–74. <https://doi.org/10.1016/j.icarus.2003.08.009>
- Pérez-Hoyos, S., Sánchez-Lavega, A., Hueso, R., García-Melendo, E., & Legarreta, J. (2009). The Jovian anticyclone BA: III. Aerosol properties and color change. *Icarus*, *203*, 516–530. <https://doi.org/10.1016/j.icarus.2009.06.024>
- Pérez-Hoyos, S., Sánchez-Lavega, A., Sanz-Requena, J. F., Barrado-Izagirre, N., Carrión-González, O., Anguiano-Arteaga, A., et al. (2020). Color and aerosol changes in Jupiter after a North Temperate Belt disturbance. *Icarus*, *132*, 114021. <https://doi.org/10.1016/j.icarus.2020.114031>
- Rogers, J. H. (1995). *The giant planet jupiter*. Cambridge, U. K. Cambridge University Press. (pp. 188–197).
- Rogers, J. H., Eichstädt, G., Jacquesson, M., Hansen, C. J., Orton, G. S., et al. (2018). The new South Tropical Disturbance and its interaction with the Great Red Spot. *European Planetary Science Congress. 12*. EPSC2018-562.
- Sada, P. V., Beebe, R. F. & Conrath, B. J. (1996). Comparison of the Structure and Dynamics of Jupiter's Great Red Spot between the Voyager 1 and 2 Encounters. *Icarus*, *119*, 311–335. <https://doi.org/10.1006/icar.1996.0022>
- Sánchez-Lavega, A. (2011). *An introduction to planetary atmospheres*. Florida: Taylor-Francis, CRC Press, (p. 629).
- Sánchez-Lavega, A. (2021). *Jupiter Great Red Spot flakes*. Figshare. Collection. <https://doi.org/10.6084/m9.figshare.c.5226206.v2>
- Sánchez-Lavega, A., García-Melendo, E., Legarreta, J., Hueso, R., del Río-Gaztelurrutia, T., et al. (2020). A complex storm system and a planetary-scale disturbance in Saturn's north polar atmosphere in 2018. *Nature Astronomy*, *4*, 180–187. <https://doi.org/10.1038/s41550-019-0914-9>
- Sánchez-Lavega, A., García-Munoz, A., del Río-Gaztelurrutia, T., Pérez-Hoyos, S., Sanz-Requena, J. F., Hueso, R., et al. (2020). Multilayer hazes over Saturn's hexagon from Cassini ISS limb images. *Nature Communications*, *11*, 2281. <https://doi.org/10.1038/s41467-020-16110-1>
- Sánchez-Lavega, A., Hueso, R., Eichstädt, G., Orton, G., Rogers, J., Hansen, C. J., et al. (2018). The rich dynamics of Jupiter's Great Red Spot from JunoCam – Juno images. *The Astronomical Journal*, *156*(9pp), 162. <https://doi.org/10.3847/1538-3881/aada81>
- Sánchez-Lavega, A., Hueso, R., Lecacheux, J., Colas, F., Rojas, J. F., Gomez, J. M., et al. (1998). Dynamics and interaction between a large-scale vortex and the Great Red Spot in Jupiter. *Icarus*, *136*, 14–26. <https://doi.org/10.1006/icar.1998.6006>
- Sánchez-Lavega, A., Legarreta, J., García-Melendo, E., Hueso, R., Pérez-Hoyos, S., et al. (2013). Colors of Jupiter's large anticyclones and the interaction of a Tropical Red Oval with the Great Red Spot in 2008. *Journal of Geophysical Research*, *118*, 1–21. <https://doi.org/10.1002/2013JE004371>
- Sánchez-Lavega, A., Orton, G. S., Morales, R., Lecacheux, J., Colas, F., Fisher, B., et al. (2001). The merger of two giant anticyclones in the atmosphere of Jupiter. *Icarus*, *149*, 491–495. <https://doi.org/10.1006/icar.2000.6548>
- Sánchez-Lavega, A., Rojas, J. F., Hueso, R., Lecacheux, J., Colas, F., Acarreta, J. R., et al. (1999). Interaction of Jovian White Ovals BC and DE in 1998 from Earth-based observations in the visual range. *Icarus*, *142*, 116–124. <https://doi.org/10.1006/icar.1999.6197>
- Simon, A. A., Tabataba-Vakili, F., Cosentino, R., Beebe, R. F., Wong, M. H., & Orton, G. S. (2018). Historical and Contemporary Trends in the Size, Drift, and Color of Jupiter's Great Red Spot. *The Astronomical Journal*, *155*(4), 13. <https://doi.org/10.3847/1538-3881/aaae01>
- Simon, A. A., Wong, M. H., & Orton, G. S. (2015). First results from the Hubble OPAL program : Jupiter in 2015. *The Astrophysical Journal*, *812*, 55. <https://doi.org/10.1088/0004-637X/812/1/55>
- Smith, B. A., Soderblom, L. A., Johnson, T. V., Ingersoll, A. P., Collins, S. A., Shoemaker, E. M., et al. (1979). The Jupiter System through the eyes of Voyager 1. *Science*, *204*, 951–972. <https://doi.org/10.1126/science.204.4396.951>
- Solberg, H. G. (1969). A 3-month oscillation in the longitude of Jupiter's Red Spot. *Planetary and Space Science*, *17*, 1573–1580. [https://doi.org/10.1016/0032-0633\(69\)90146-9](https://doi.org/10.1016/0032-0633(69)90146-9)
- Soria, M., García-Melendo, E., & Prat, A. (2020). *Shallow water model, shallow Worlds 2*. Zenodo. <https://doi.org/10.5281/zenodo.4312681>
- Taylor, F. W., Atreya, S. K., Encrenaz, T., Hunten, D. M., Irwin, P. G. J., & Owen, T. C. (2004). *The composition of the atmosphere of Jupiter*. In F. Bagenal, T. E. Dowling, & W. B. McKinnon (Eds.), Eds., *Jupiter: The planet, satellites and magnetosphere*, Vol. 1, (pp. 59–78).
- Trigo-Rodríguez, J. M., Sánchez-Lavega, A., Gómez, J. M., Lecacheux, J., Colas, F., & Miyazaki, I. (2000). The 90-day oscillations of Jupiter's Great Red Spot revisited. *Planetary and Space Science*, *48*, 331–339. [https://doi.org/10.1016/S0032-0633\(00\)00002-7](https://doi.org/10.1016/S0032-0633(00)00002-7)
- Tur, A., & Yanovsky, V. (2017). *Coherent vortex structures in fluids and plasmas*. Springer ed. Springer Series in Synergetics. <https://doi.org/10.1007/978-3-319-52733-8>
- Vasavada, A. R., & Showman, A. P. (2005). Jovian atmospheric dynamics: An update after Galileo and Cassini. *Reports on Progress in Physics*, *68*, 1935–1996. <http://dx.doi.org/10.1088/0034-4885/68/8/R06>
- Wang, Y., & Holland, G. (1996). The beta drift of baroclinic vortices. Part I: adiabatic vortices. *Journal of the Atmospheric Sciences*, *53*, 411–427. [https://doi.org/10.1175/1520-0469\(1996\)053<0411:TBD0BV>2.0.CO;2](https://doi.org/10.1175/1520-0469(1996)053<0411:TBD0BV>2.0.CO;2)
- WinJUPOS. (2020). *Sample implementation of version 3*. Astronomical Publications. Retrieved from <http://www.grischa-hahn.home-page.t-online.de/>
- Wong, M., de Pater, I., Simon, A. A., & Marcus, P. S. (2019). *Jupiter's Great red spot is not disintegrating by flaking apart*. San Francisco. American Geophysical Union Fall Meeting. Poster P13B-3502.